

# Deep Video Restoration for Under-Display Camera

Xuanxi Chen<sup>1</sup>, Tao Wang<sup>1</sup>, Ziqian Shao<sup>1</sup>, Kaihao Zhang<sup>2</sup>, Wenhan Luo<sup>3</sup>, Tong Lu<sup>1</sup>,  
Zikun Liu<sup>4</sup>, Tae-Kyun Kim<sup>5</sup>, Hongdong Li<sup>2</sup>

<sup>1</sup>State Key Lab for Novel Software Technology, Nanjing University, China

<sup>2</sup>Australian National University, Australia

<sup>3</sup>Shenzhen Campus of Sun Yat-sen University, China

<sup>4</sup>Samsung Research China-Beijing (SRC-B), China

<sup>5</sup>Imperial College London, UK

{xxchen.nju, taowangzj, super.khzhang, whluo.china, hongdong.li}@gmail.com, ziqian.shao@outlook.com,  
lutong@nju.edu.cn, zikun.liu@samsung.com, tk.kim@imperial.ac.uk,

## Abstract

Images or videos captured by the Under-Display Camera (UDC) suffer from severe degradation, such as saturation degeneration and color shift. While restoration for UDC has been a critical task, existing works of UDC restoration focus only on images. UDC video restoration (UDC-VR) has not been explored in the community. In this work, we first propose a GAN-based generation pipeline to simulate the realistic UDC degradation process. With the pipeline, we build the first large-scale UDC video restoration dataset called PexelsUDC, which includes two subsets named PexelsUDC-T and PexelsUDC-P corresponding to different displays for UDC. Using the proposed dataset, we conduct extensive benchmark studies on existing video restoration methods and observe their limitations on the UDC-VR task. To this end, we propose a novel transformer-based baseline method that adaptively enhances degraded videos. The key components of the method are a spatial branch with local-aware transformers, a temporal branch embedded temporal transformers, and a spatial-temporal fusion module. These components drive the model to fully exploit spatial and temporal information for UDC-VR. Extensive experiments show that our method achieves state-of-the-art performance on PexelsUDC. The benchmark and the baseline method are expected to promote the progress of UDC-VR in the community, which will be made public.

## Introduction

Recently, under-display camera (UDC) technology has made it a popular trend to enable bezel-free and notch-free viewing experiences on devices such as smartphones, TV, laptops, and tablets. However, the display embedded in the front of the camera directly leads to saturation degeneration, color shift, and contrast reduction in the captured images using UDC (Zhou et al. 2021; Feng et al. 2021). Restoration under UDC has become a newly-defined task that aims to recover visually pleasing results from degraded inputs.

To address this problem, recent methods focus on image restoration for UDC. For example, Zhou et al. (2021) first analyze the UDC imaging process and propose two real UDC image datasets (TOLED and POLED) by a monitor-camera image system. Feng et al. (2021) build a synthetic dataset



Figure 1: Some examples from our proposed PexelsUDC. The bottom row is the clean video sequence. The top and middle rows are sequences sampled from PexelsUDC-T and PexelsUDC-P, respectively. Zoom in for a better view.

using the measured point spread function to simulate UDC degraded images, which focuses on diffraction artifacts in HDR images. Some methods (Sundar et al. 2020; Zhou et al. 2021; Kwon et al. 2021; Feng et al. 2021; Koh, Lee, and Yoon 2022; Feng et al. 2023) resort to different deep learning architectures such as dynamic skip connection network (Feng et al. 2021), two-branched network (Koh, Lee, and Yoon 2022) to recover clear images in an end-to-end manner. Although these image-based methods work well in processing degraded UDC images, they are sub-optimal to video restoration in UDC. The image-based methods do not consider the inherent temporal information in the video. On the other hand, existing video restoration methods that utilize temporal cues are not specifically tailored for UDC restoration tasks, thereby overlooking the unique characteristics of UDC videos.

To our best knowledge, few studies have explored UDC Video Restoration (UDC-VR) in the community so far. There are two major unresolved issues that hinder the progress of this task in the community. The first one is the lack of a public and standard benchmark. Till now, there is no benchmark dataset for UDC-VR tasks, which makes it difficult to understand and explore this task in depth. In addition, there exist UDC image datasets, while their scale is small and inherently lacks temporal cues. The second is the lack of baseline algorithms for this task. When a new method is proposed, the authors have to retrain other video restoration methods to achieve a fair comparison, which is effort-demanding.

To advance the development of UDC-VR, we make the first attempt to investigate the UDC-VR problem in this work. To begin with, we propose an automatic pipeline called the

UDC video generation pipeline to establish a large-scale video benchmark for UDC-VR. Specifically, the proposed pipeline contains four stages: *video collection*, *manual filtering*, *GAN-based UDC video generation*, and *artifact elimination and selection*. In our pipeline, the first two phases are used to collect high-quality videos, and the latter two phases are designed to synthesize the corresponding UDC videos. Among them, the GAN-based UDC video generation is the core stage. We propose a generative model to learn the realistic degradation of UDC from the datasets TOLED and POLED (Zhou et al. 2021) which are collected in real scenes. On the basis of our video generation pipeline, we build the first UDC video dataset called PexelsUDC for UDC-VR. PexelsUDC consists of two subsets named PexelsUDC-T and PexelsUDC-P related to different displays for UDC. Each subset contains 160 videos, with 140 videos allocated for training and 20 videos designated for testing purposes. Each individual video comprises 100 successive frames, all with a resolution of  $1280 \times 720$ . We show some examples in Fig. 1.

Based on our PexelsUDC, we first conduct extensive benchmark studies on existing mainstream image/video restoration methods and then we propose a new UDC-VR baseline method (Video Transformer for UDC) called VTUDC for the UDC-VR task. VTUDC is a transformer-based network with two branches. Specifically, VTUDC first adopts a spatial branch and a temporal branch in parallel to extract spatial and temporal cues from the input video, respectively. Then the extracted spatial-temporal information is integrated and enhanced by a spatial-temporal fusion module (STFM), which helps the network to dynamically emphasize the complementarity between spatial and temporal information. After that, the fused feature will pass through stacked spatial transformer blocks to be enhanced again. Finally, the feature is projected to the same size as the reference frame by a convolution with the PixelShuffle (Shi et al. 2016) operation, and the restored reference frame is obtained by residual connection with the reference frame. Experimental results show that VTUDC achieves state-of-the-art results on both PexelsUDC-T and PexelsUDC-P.

In summary, our main contributions are threefold: (1) We build a new high-quality UDC dataset for video restoration. To the best of our knowledge, it is the first large-scale UDC video dataset in the literature. In addition, we benchmark five state-of-the-art video restoration methods on the two datasets. It helps understand the potential and limitations of these methods on UDC video restoration. (2) We propose a new transformer-based method, VTUDC, for UDC video restoration. For the newly-defined UDC video restoration task, this serves as a baseline method. VTUDC leverages the characteristics of UDC videos and thus extracts spatio-temporal features more effectively. (3) Comprehensive experiments on two subsets of our dataset demonstrate that VTUDC achieves not only state-of-the-art quantitative performance but also consistently superior perceptual quality.

## Related Work

**UDC Image Restoration.** Zhou et al. (2021) propose two methods to tackle UDC image restoration on TOLED and POLED dataset, which are a conventional method using

Wiener Filter (Goldstein, Reed, and Scharf 1998) and a learning-based method with U-shape architecture. DISC-Net (Feng et al. 2021) utilizes dynamic convolution and uses the provided PSFs as extra knowledge to guide the model. BNUDC (Koh, Lee, and Yoon 2022) is a two-branched DNN that considers high-spatial-frequency and low-spatial-frequency degradation for UDC image restoration.

**UDC Datasets and Simulation.** Zhou et al. (2021, 2020) employ a Monitor-Camera Imaging System (MCIS) system to collect paired and aligned realistic data (TOLED and POLED datasets). Feng et al. (2023) specifically design AlignFormer to address misalignment problems in the real collected data. Since the scale of realistic UDC datasets are usually small, and the real paired UDC data is difficult to obtain, (Feng et al. 2021, 2022) propose a model-based synthesis pipeline based on measured PSF to generate a large-scale synthetic UDC dataset. Many works also use GANs to simulate UDC images in TOLED and POLED for data augmentation in UDC image restoration. However, the performance of the simulation is not ideal for generating UDC datasets. The glass simulation in DAGF-GAN (Sundar et al. 2020) introduces different noise patterns at the image’s edge. MPGNet (Zhou, Song, and Du 2022) integrates the realistic noise estimation module in GAN for end-to-end training. However, the noise in the original data set is a fixed pattern which is read-shot noise. Meanwhile, the synthetic results of MPGNet differ from TOLED and POLED in detail. We propose a two-stage UDC synthetic pipeline to learn real UDC degradation, decoupling noise estimation from an end-to-end learning framework. To our knowledge, no publicly available UDC video dataset has been available, and one of our main contributions is proposing the first UDC video dataset PexelsUDC based on our UDC synthetic pipeline.

**Video Restoration with Transformer.** Transformer is first introduced by Vaswani et al. (2017) in natural language processing tasks. Then broad ranges of development based on transformers are introduced to high-level vision tasks (Dosovitskiy et al. 2021; Carion et al. 2020; Zhu et al. 2021; Wang et al. 2021; Touvron et al. 2021; Liu et al. 2021) and low-level vision tasks (Chen et al. 2021; Liang et al. 2021; Wang et al. 2022). Transformer has also been introduced for video restoration (Kim et al. 2018; Liang et al. 2022; Zheng et al. 2022; Geng et al. 2022; Lin et al. 2022; Luo et al. 2022). Inspired by Swin Transformer (Liu et al. 2021; Liang et al. 2021), more video restoration methods have adopted window-based multi-head attention in recent years. Zheng et al. (2022) adopt SwinIR (Liang et al. 2021) as their backbone model in the second stage. RSTT (Geng et al. 2022) exploits the stacked Swin Transformer Block to solve the video super-resolution problem. FGST (Lin et al. 2022) modifies the original window-based local self-attention to use the guidance of optical flow to expand the receptive field. BSRT (Luo et al. 2022) incorporates Swin Transformer blocks to better use inter-frame information.

## PexelsUDC Dataset

### UDC Degradation Model

As TOLED and POLED are real-world collected paired datasets, thus we try to simulate the degradation existing

in these datasets. We follow the degradation model proposed by Zhou et al. (2021) and extend it to the video domain. The degradation model of the  $t$ -th frame in UDC videos can be defined as:

$$y_t = (\gamma * x_t) \otimes k + n, \quad (1)$$

where  $y$  is the degraded video frame,  $x$  is the clean frame,  $k$  is the point spread function (PSF),  $\gamma$  is the scale factor that indicates the attenuation of light intensity,  $n$  is additive noise, and  $\otimes$  represents the convolution operator. It should be noted that  $\gamma$ ,  $k$ , and  $n$  are usually fixed because they are parameters related to the imaging system.

## Two-Stage Simulation Pipeline

Based on the above degradation model, we propose a two-stage generation method to learn the degradation of UDC. The overall architecture of our method is shown in Fig. 2. The details of two-stage of our methods are shown as follows:

**Degradation Learning via GAN Model.** We adopt GAN to learn the degradation from UDC images in PexelsUDC. For the generator, the main body is a customized U-shaped network (Ronneberger, Fischer, and Brox 2015). Inspired by (Zhou, Song, and Du 2022), we also design a light attenuation module and put it in front of the U-shape network to facilitate the generation. See Supp. Material for more details about the model. For the discriminator, we use PatchGAN discriminator (Isola et al. 2017), which has been proven to be effective in image-to-image translation fields.

**Additive Noise.** Zhou et al. (2021) adopt a simple noise model following the commonly used read-shot noise, which can be formulated as a heteroscedastic Gaussian:

$$n(x) \sim N(\mu = 0, \sigma^2 = \lambda_{read} + \lambda_{shot}x), \quad (2)$$

where the mean value is 0, and the variance is signal-dependent.  $\lambda_{read}$  and  $\lambda_{shot}$  are parameters related to the camera. Due to the fixed noise pattern, we do not include a noise learning module in our GAN. Thus, at the end of stage 1 in Fig. 2, the image generated by GAN does not contain noise. Since  $\lambda_{read}$  and  $\lambda_{shot}$  are not available, and we do not have pairs of images with and without noise for training, we manually set some candidate values for  $\lambda_{read}$  and  $\lambda_{shot}$ . To determine  $\lambda_{read}$  and  $\lambda_{shot}$ , twenty volunteers were recruited to rate how close the generated images were to real images under each set of parameters. Furthermore, temporal coherence is crucial for synthetic video datasets. UDC degradation differs from other degradation, such as rain, haze, and snow. UDC degradation originates from the imaging system rather than the environment captured in the image, so once we have effectively learned the characteristics of UDC degradation, we possess a "camera lens" for UDC. Hence, stable GAN outputs can ensure temporal coherence at moderate frame rates. We choose moderate videos with moderate frame rates to alleviate this problem.

## Our PexelsUDC

Based on the UDC simulation pipeline, we propose a high-quality and large-scale benchmark dataset PexelsUDC considering two kinds of degradation (TOLED and POLED) for UDC-VR. To obtain the source clean videos, we resort to

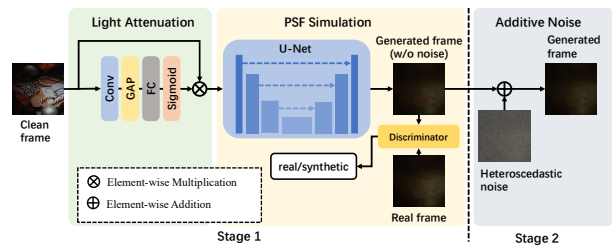


Figure 2: The structure of our two-stage simulation pipeline. The first stage is a GAN that learns the light attenuation and PSF. The second stage is adding heteroscedastic noise to the generated frame of the first stage.

Pexels<sup>1</sup>, where all the videos are free to use. The ground-truth videos we collected are all real shots taken by different smart devices, which include a variety of content like people, animals, natural scenery, *etc.* The FPS of videos in our dataset is relatively moderate, between 25 and 50. In PexelsUDC, there are 140 pairs of videos for training and 20 pairs for testing. All the videos are of  $1280 \times 720$  resolution, and each sequence has 100 frames. See Supp. Material for more information about our PexelsUDC.

## Proposed Method

As shown in Fig. 3, VTUDC is a two-branch transformer-based method. Given  $2N + 1$  degraded frames, the parallel **spatial and temporal branches** first process the input reference frame and video frames to capture spatial and temporal information. Then, the features produced by these two branches are fused and enhanced via a **spatial-temporal fusion module**. Finally, the features are recovered into the clear reference frame  $N$ . We discuss these core components of VTUDC as follows.

### Spatial Branch

Through the comprehensive analysis of UDC image degradation, we find that blur and noise are the main degradation factors of the UDC restoration task. Considering the local information is helpful for blur and noise removal (Zhou, Song, and Du 2022), we thus resort to using the local-aware transformer block as one basic unit to build the spatial branch of the network. As illustrated in Fig. 3, the spatial branch contains one shallow feature extractor and several stacked local-aware transformer blocks. The extractor is used to extract shallow features from the input reference frame, and the stacked local-aware transformer blocks are designed to guide the network to focus on local information for UDC restoration. As the local-aware transformer block is our core component, we discuss it as follows.

Recent transformer networks have shown significant performance improvements on low-level vision tasks. However, the transformer structure usually conducts global self-attention, which may not be suitable for the UDC video restoration task. Thus, motivated by Liu et al. (2021), we introduce the window-based mechanism in the self-attention to build a local-aware transformer block. Compared with

<sup>1</sup><https://www.pexels.com/>

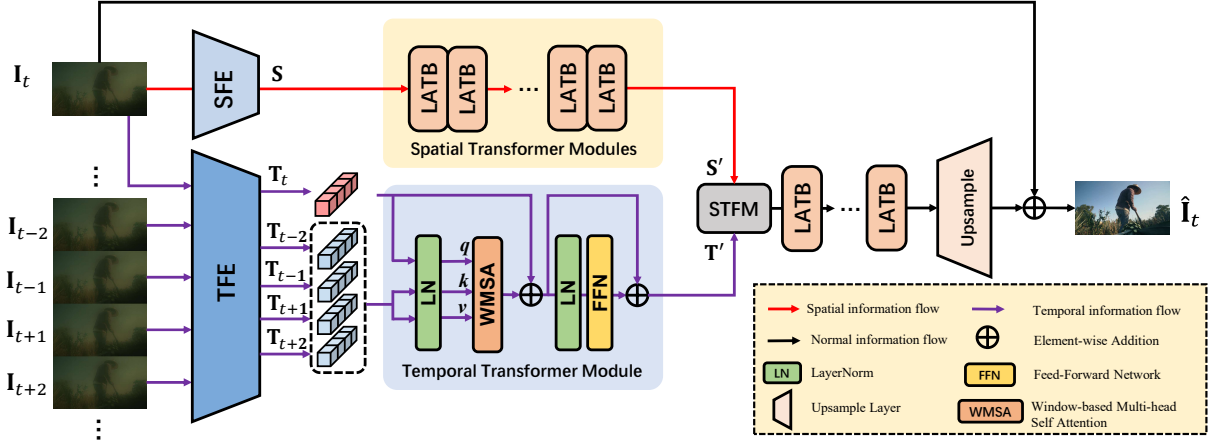


Figure 3: The overall structure of proposed VTUDC. The reference frame is sent into the spatial branch. It passes through Spatial Feature Extractor (SFE) to get the shallow spatial feature  $S$ . Then stacked Local-Aware Transformer Blocks (LATB) are adopted to obtain the spatial feature  $S'$ . The video sequence is sent into the temporal branch where the feature of each frame is first extracted by Temporal Feature Extractor (TFE). Then the features of frames are fed into Temporal Transformer Module to obtain the temporal feature  $T'$ . Then  $S'$  and  $T'$  are fused together by the Spatial-Temporal Fusion Module (STFM) and enhanced by following stacked LATBs. The structure of STFM and LATBs are shown in Fig. 4.

the original ViT (Dosovitskiy et al. 2021), window-based self-attention focuses more on local information and reduces the computational complexity, which can better help blur and noise removal for the UDC restoration task. Suppose the input feature is  $\mathbf{X} \in \mathbb{R}^{C \times H \times W}$ . In the local-aware transformer block,  $\mathbf{X}$  is first divided into non-overlapping windows:  $\mathbf{X} \rightarrow \{\mathbf{X}_1, \mathbf{X}_2, \dots, \mathbf{X}_n\}$ ,  $n = HW/M^2$  with the window size of  $M \times M$ , where  $n$  is the total number of windows. In addition, we apply the learnable absolute position embedding on feature  $\mathbf{X}_i$  of each window. Then the feature maps of each window are flattened and transposed into the shape of  $\mathbb{R}^{M^2 \times C}$ . After that, we perform multi-head self-attention in each window independently. For each window, let the head number be  $k$ , and the head dimension be  $d = C/k$ , the query, key, and value under the  $k$ -th head self-attention are generated as follows:

$$\mathbf{Q}_i = \mathbf{X}_i \mathbf{W}_Q, \quad \mathbf{K}_i = \mathbf{X}_i \mathbf{W}_K, \quad \mathbf{V}_i = \mathbf{X}_i \mathbf{W}_V, \quad (3)$$

where  $\mathbf{W}_Q, \mathbf{W}_K, \mathbf{W}_V \in \mathbb{R}^{C \times d}$  represent the projection matrices of query, key, and value, respectively. The formulation for attention is:

$$\text{Attention}(\mathbf{Q}, \mathbf{K}, \mathbf{V}) = \text{Softmax}\left(\frac{\mathbf{Q}\mathbf{K}^T}{\sqrt{d}}\right)\mathbf{V}. \quad (4)$$

Next, the feature passes through the feed-forward network (FFN). FFN consists of two fully-connected (FC) layers, each layer is followed by a GELU activation function. The whole process of the local-aware block is formulated as follows:

$$\begin{aligned} \mathbf{X}' &= \text{MHSA}(\text{FFN}(\text{LN}(\text{PE}(\mathbf{X})))) + \mathbf{X}, \\ \mathbf{X}'' &= \text{FFN}(\text{LN}(\mathbf{X}')) + \mathbf{X}', \end{aligned} \quad (5)$$

where LN indicates the LayerNorm (Ba, Kiros, and Hinton 2016) layer, and PE is the patch embedding. We illustrate the structure of the local-aware block in Fig. 4 (a). In addition, we also utilize the shifted window mechanism in these stacked local-aware transformer blocks to further enhance the long-range dependency modeling capacities of the spatial branch.

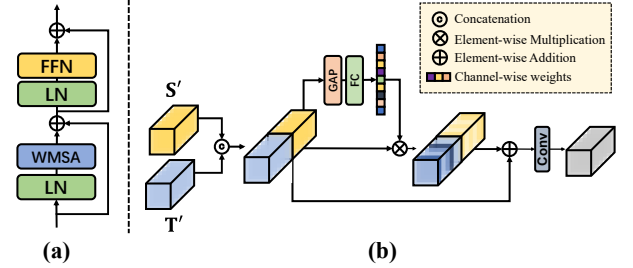


Figure 4: (a) Local-Aware Transformer Block (LATB). (b) Spatial-Temporal Fusion Module (STFM). LN is the LayerNorm. FFN is the feed-forward network. WMSA is window-based multi-head self-attention.

## Temporal Branch

In contrast to UDC image restoration, UDC-VR is more challenging because it is not clear how to utilize the inherent temporal information in successive video frames to assist the restoration process. Thus, we propose a temporal branch in the network to exploit the temporal information from input videos. Specifically, the temporal branch consists of a U-shaped feature extractor composed of a local-aware transformer block and a temporal transformer module. The feature extractor is used to transform input frames into features, and the temporal transformer module is adopted to seek complementary sharp information existing in neighboring frames. The structure of Temporal Transformer is shown in Fig. 3. Specifically, given the feature maps  $\mathbf{T} \in \mathbb{R}^{K \times C \times H' \times W'}$  after feature extraction, the feature maps are split into non-overlapping windows with the size of  $M_t \times M_t$ . Then the feature maps of each window  $j$  in frame  $i$  will be flattened and transposed to obtain  $\mathbf{T}_{i,j} \in \mathbb{R}^{M_t^2 \times C}$ . In this way, features of every frame  $\mathbf{T}_i$  is in the shape of  $\mathbb{R}^{M_t^2 \times \frac{H'W'}{M_t^2} \times C}$ . The feature of the reference frame  $\mathbf{T}_t$  is sent into the multi-head self-attention module as the query, and the features of

Table 1: The effectiveness of our GAN-based UDC generation method. We train DWFormer (Zhou, Song, and Du 2022) on three different datasets: Original data, Data-MPGNet, and Data-Ours. The original data refers to the testing sets of TOLED and POLED, while Data-MPGNet and Data-Ours are generated by MPGNet and our method, respectively. The best and second-best results are marked in bold and underlined respectively.

Training Dataset	TOLED-Val				POLED-Val			
	PSNR $\uparrow$	SSIM $\uparrow$	LPIPS $\downarrow$	DISTS $\downarrow$	PSNR $\uparrow$	SSIM $\uparrow$	LPIPS $\downarrow$	DISTS $\downarrow$
Original data	<b>31.52</b>	<b>0.8723</b>	<b>0.3605</b>	<b>0.1920</b>	<b>21.23</b>	<b>0.6880</b>	<b>0.5391</b>	<b>0.3417</b>
Data-MPGNet	28.97	0.8269	0.3830	0.2912	16.86	0.5780	0.5580	0.3721
Data-Ours	<u>30.49</u>	<u>0.8568</u>	<u>0.3780</u>	<u>0.2203</u>	<u>20.77</u>	<u>0.6340</u>	<u>0.5498</u>	<u>0.3702</u>

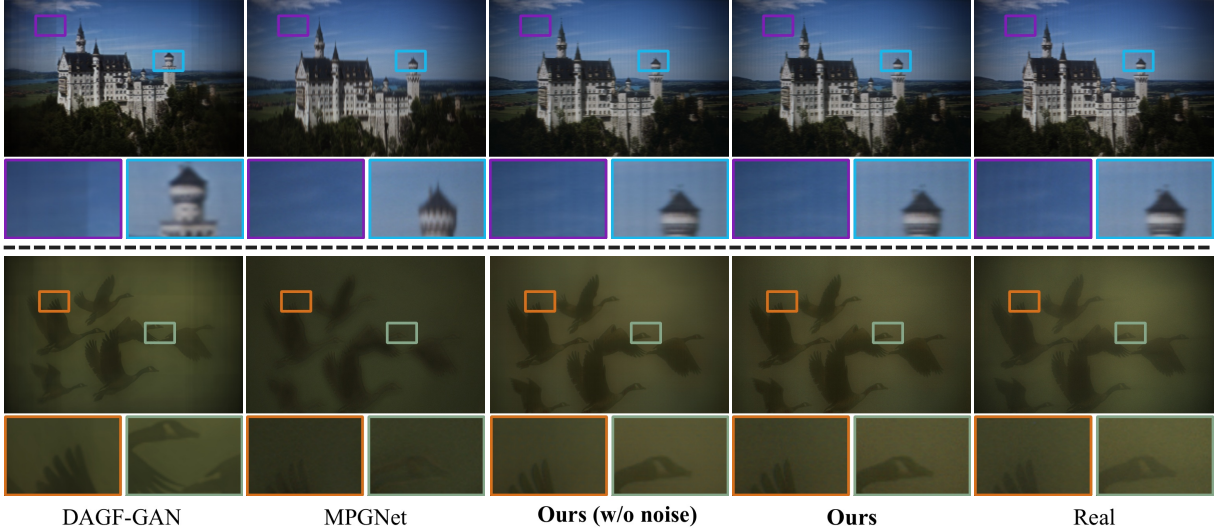


Figure 5: Generation comparison on TOLED and POLED validation sets. The top row shows TOLED validation results, and the bottom row shows POLED validation results. DAGF-GAN (Sundar et al. 2020) is trained on original images from DIV2K (Agustsson and Timofte 2017) which are misaligned with images in TOLED and POLED. Official pre-trained models of DAGF-GAN and MPGNet are adopted.

neighboring frames are treated as the key and value. Then we perform the multi-head self-attention described in Eqn. 4 to derive the final temporal feature  $\mathbf{T}' \in \mathbb{R}^{C \times H' \times W'}$ . Compared to previous works using optical flow (Lin et al. 2022) or deformable convolution (Wang et al. 2019) to model temporal information, our temporal transformer is simple and can directly improve restoration performance.

### Spatial-Temporal Fusion Module

After obtaining information from the spatial and temporal domains, we need to fuse them together. It is necessary to choose between spatial and temporal information and emphasize the useful information in the features of both spatial and temporal parts. Therefore, we propose a spatial-temporal fusion module, where channel attention is adopted to re-weight the features from two branches. The structure of STFMs is shown in Fig. 4 (b).

The feature map  $\mathbf{S}' \in \mathbb{R}^{C \times H' \times W'}$  from the spatial branch and  $\mathbf{T}' \in \mathbb{R}^{C \times H' \times W'}$  from the temporal branch are first concatenated together which is denoted by  $\mathbf{F} \in \mathbb{R}^{2C \times H' \times W'}$ . Then  $\mathbf{F}$  passes through the global average pooling (GAP) and a fully-connected (FC) layer to derive the weights  $\mathbf{W} \in \mathbb{R}^{2C \times 1 \times 1}$  for every channel in  $\mathbf{F}$  which is a channel attention (CA) operation. Then we multiply  $\mathbf{F}$  and  $\mathbf{W}$  and make the residual connection with  $\mathbf{F}$ . Then the features are

downsampled to obtain the fused feature  $\mathbf{F}' \in \mathbb{R}^{C \times H' \times W'}$ . This process can be formulated as:

$$\begin{aligned} \text{CA}(\mathbf{F}) &= \text{FC}(\text{GAP}(\mathbf{F})) * \mathbf{F}, \\ \mathbf{F}' &= \text{Conv}(\text{CA}(\mathbf{F})) + \mathbf{F}. \end{aligned} \quad (6)$$

Then  $\mathbf{F}'$  passes through the stacked local-aware transformer blocks to be enhanced. Finally,  $\mathbf{F}$  is projected to the same size as the reference frame, taken as residual, and added to itself to derive the restored reference frame.

## Experiments

### Experimental Settings

We train our GAN-based model on both TOLED and POLED (Zhou et al. 2021) separately. As to the data augmentation, random cropping ( $512 \times 512$  patches) and flipping (both horizontal and vertical) are used. The generator and discriminator are optimized by Adam (Kingma and Ba 2014) where  $\beta_1 = 0.5$  and  $\beta_2 = 0.999$ . The initial learning rate is set to  $4 \times 10^{-4}$  and the batch size is set to 1.

**UDC-VR.** VTUDC receives 5 consecutive frames as input. For data augmentation, random cropping ( $256 \times 256$  patches) and flipping (both horizontal and vertical) are adopted. All the modules are trained with the Adam optimizer where  $\beta_1 = 0.9$  and  $\beta_2 = 0.99$ . The initial learning rate is set to  $4 \times 10^{-4}$  and the batch size is set to 2. We train VTUDC using both

Table 2: UDC-VR results on PexelsUDC. The best and second-best results are marked in bold and underlined, respectively.

Methods	PexelsUDC							
	PexelsUDC-T				PexelsUDC-P			
	PSNR $\uparrow$	SSIM $\uparrow$	LPIPS $\downarrow$	DISTS $\downarrow$	PSNR $\uparrow$	SSIM $\uparrow$	LPIPS $\downarrow$	DISTS $\downarrow$
DWFormer	31.61	0.8903	0.2610	0.1185	24.91	0.7901	0.3879	0.1729
DAGF	30.75	0.8693	0.2636	0.1226	27.99	0.8321	0.3580	0.1667
DBN	31.70	0.8942	0.2474	0.1087	27.96	<u>0.8552</u>	<u>0.3178</u>	<u>0.1349</u>
EDVR	<u>32.33</u>	0.8778	0.2678	<u>0.0936</u>	27.70	0.8122	0.3846	0.1486
DBLRNet	32.21	0.8999	0.2462	0.1016	<b>28.03</b>	0.8441	0.3533	0.1424
IFI-RNN	32.29	<u>0.9022</u>	<u>0.2362</u>	0.1067	27.68	0.8530	0.3278	0.1443
FGST	31.75	0.8939	0.2592	0.1164	24.92	0.7790	0.4358	0.1743
<b>Ours</b>	<b>33.61</b>	<b>0.9187</b>	<b>0.2016</b>	<b>0.0856</b>	<u>28.01</u>	<b>0.8645</b>	<b>0.2966</b>	<b>0.1255</b>

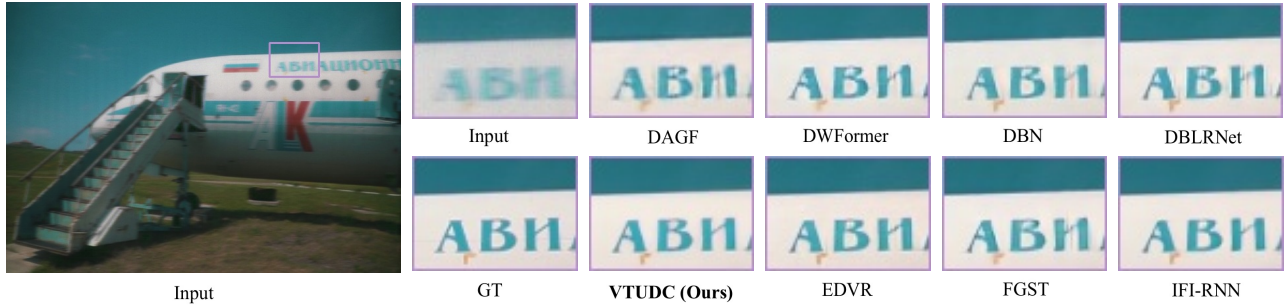


Figure 6: Exemplar results on the subset PexelsUDC-T from PexelsUDC. The image restored by VTUDC is clearer and contains fewer artifacts. Zoom in for a better view.

Charbonnier loss (Charbonnier et al. 1994) and Perceptual loss (Johnson, Alahi, and Fei-Fei 2016) with the weight 1 and  $1 \times 10^{-4}$ , respectively. VTUDC are trained with four NVIDIA V100 GPUs with 32G memory.

**Evaluation metrics.** For both UDC image generation and UDC-VR, we adopted PSNR, SSIM (Wang et al. 2004), LPIPS (Zhang et al. 2018b) and DISTS (Ding et al. 2020) to make a comprehensive comparison. PSNR and SSIM are pixel-wise metrics. LPIPS and DISTS are perceptual metrics.

### UDC Generation Analysis

We choose two existing UDC simulation methods for comparison, which are DAGF-GAN (Sundar et al. 2020) and MPGNet (Zhou, Song, and Du 2022). We test all UDC generation models on TOLED and POLED validation sets. Quantitative results (See Supp. Material) show that our method outperforms the existing UDC simulation methods on all metrics. The visualization results are demonstrated in Fig. 5. For both TOLED and POLED, the images generated by DAGF-GAN show different patterns at the edges compared to real degraded images, and there is no evident noise in the images as DAGF-GAN does not consider noise. MPGNet has a module specifically for noise and thus achieves better performance than DAGF-GAN. However, MPGNet still suffers from the following problems. First, it fails to generate the periodic bands in TOLED. Second, the degradation learned by MPGNet deviates from the true TOLED in detail. As shown in Fig. 5, the spire of the tower generated by MPGNet shows different patterns from the real one evidently. Our GAN-based model outperforms the other two methods, where the generated images are much closer to the real UDC image. In particular, we can delineate fine details such as diffraction

haze in POLED and banded periodic noise in TOLED.

In addition, we conduct training of DWFormer (Zhou, Song, and Du 2022) using three distinct settings. Firstly, we use the original testing set of TOLED and POLED as the original data and generate UDC images by using GT images from the original data through both MPGNet and our method. Following this, DWFormer is trained separately using these three sets of data. Then, we evaluate the trained DWFormers on the validation set of TOLED and POLED. Tab. 1 demonstrates that the identical model trained on the data generated by our method outperforms the model trained on the synthesized data utilizing the MPGNet method. Moreover, it almost approaches the results of training with genuine UDC images, showcasing the effectiveness of our approach.

### Results for UDC-VR

Since there is no previous method for UDC video restoration, we select two UDC image restoration methods and several representative video restoration methods for comparison. For UDC image restoration methods, we select **DAGF** (Sundar et al. 2020) and **DWFormer** (Zhou, Song, and Du 2022). For video methods, we choose **DBN** (Su et al. 2017), **DBLRNet** (Zhang et al. 2018a), **EDVR** (Wang et al. 2019), **IFI-RNN** (Nah, Son, and Lee 2019) and **FGST** (Lin et al. 2022). For a fair comparison, all methods are retrained using the official settings, with the only variation being the number of training epochs, which is set to 500 for all methods.

The quantitative results are reported in Tab. 2. On PexelsUDC-T, VTUDC achieves the best performance of restoration under all metrics. Specifically, VTUDC has an advance of 1.28dB and 0.0165 than the second-best methods in terms of PSNR and SSIM. On PexelsUDC-P, VTUDC

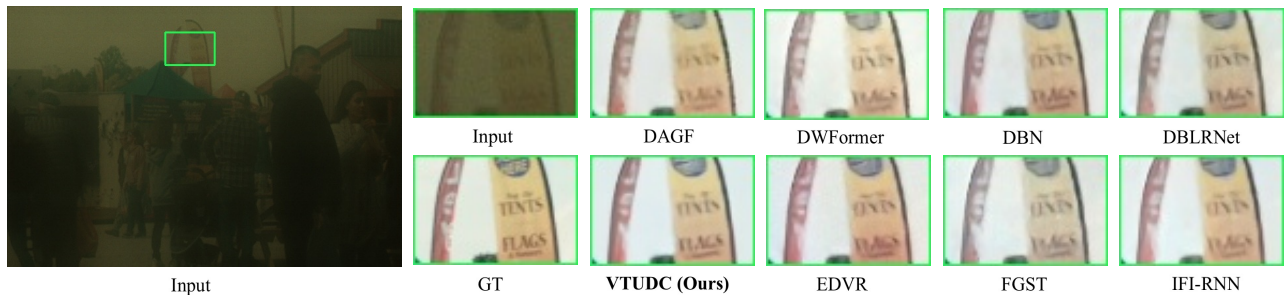


Figure 7: Exemplar results on the subset PexelsUDC-P from PexelsUDC. The details restored by VTUDC are sharper and the noise is removed. Zoom in for a better view.

Table 3: The EPE results. The lower indicator is better.

Method	Ours	DBLRNet	DWFormer
TOLED	<b>1.0578</b>	1.2375	1.2820
POLED	<b>1.9387</b>	2.1098	3.5435

Table 4: Ablation studies on branches of VTUDC.

Spatial branch	Temporal Branch	PSNR $\uparrow$ /SSIM $\uparrow$
✓		31.96/0.8903
	✓	32.15/0.9045
✓	✓	<b>33.59/0.9193</b>

achieves the highest SSIM value and the second-best PSNR, and it ranks first on both LPIPS and DISTs. The distance between VTUDC and the best DBLRNet (Zhang et al. 2018a) in PSNR is only 0.02dB. The visualization results are shown in Fig. 6 and Fig. 7. For PexelsUDC-T, VTUDC achieves better performance where the letters are well restored. In PexelsUDC-P, the results of VTUDC are clearer. In addition, VTUDC restores faithful details and removes the noise compared to other methods. In addition, to verify the temporal stability of the videos restored by our method, we used a pre-trained SPyNet (Ranjan and Black 2017) to calculate the optical flow of the model’s predicted frames and the ground truth frames. Then we calculate the endpoint error (EPE) between the optical flow of the restored video and the ground truth video. We chose two representative methods (video-based method DBLRNet and image-based method DWFormer) for comparison. The experiment results in Tab. 3 show that our method can achieve better temporal stability.

## Ablation Studies

For ablation experiments, we train all models for 300 epochs on PexelsUDC-T, and other settings are not changed.

**Two branches vs. Single branch.** We explore the effect of the two-branch structure. We remove only one branch at a time and add numbers of Spatial Transformer Blocks to keep the parameters similar to the two-branch one. The results are reported in Tab. 4. It is observed that using both spatial and temporal information is important for UDC-VR.

**Spatial-temporal fusion module.** In this part, we explore the way in which the information of the two branches are fused and the results are shown in Tab. 5. We use two other modules to replace STFM, which are directly adding the information from the two branches (denoted as Addition) and concatenating first and then passing through the convolutional layer (denoted as Concat). The results show that STFM can improve the performance of VTUDC for 0.56 dB compared with using Concat operation. **The selection mode of query,**

Table 5: Ablation studies on feature fusion.

Fusion way	Addition	Concat	STFM
PSNR $\uparrow$	32.45	33.03	<b>33.59</b>
SSIM $\uparrow$	0.9036	0.9104	<b>0.9193</b>

Table 6: Ablation studies on the selection modes of query, key, and value in Temporal Transformer.

Mode	Model (1)	Model (2)	Ours
PSNR $\uparrow$	33.12	32.99	<b>33.59</b>
SSIM $\uparrow$	0.9126	0.9128	<b>0.9120</b>

**key, and value.** We investigate how query, key, and value are selected in Temporal Transformer. We used two other selection modes for comparison: 1)  $\mathbf{F}_t$  as query,  $\mathbf{F}_{t+i}$  as key and value. 2)  $\mathbf{F}_{t+i}$  as query, key and value. The ablated results are shown in Tab. 6, indicating that the validity of information extracted by both settings is weaker than the way we adopt currently, and the latter is inferior to the former. This suggests that performance will reduce when the feature of the reference frame is involved in key and value, verifying the effectiveness of our Temporal Transformer.

**Window size for Temporal Transformer.** We change the window size in Temporal Transformer. VTUDC works best with a  $4 \times 4$  window ( $1 \times 1$ : 32.90/0.9108,  $2 \times 2$ : 32.98/0.9130,  $4 \times 4$ : **33.59/0.9193**,  $8 \times 8$ : 33.05/0.9135 in PSNR/SSIM). A too-small window may ignore some useful information embedded in neighboring frames, while a too-large window may involve interference information from neighboring frames when motion changes greatly.

## Conclusion

In this paper, we explore the UDC video restoration task which has not been studied in the community. We propose a UDC video generation pipeline where high-quality UDC videos can be generated. Based on this pipeline, we construct the first dataset for UDC video restoration. For this new task, we design a transformer-based method (VTUDC) of a two-branch structure to tackle it. With the exploitation of both spatial and temporal cues, VTUDC achieves better performance than other video restoration methods on the proposed dataset both quantitatively and qualitatively. All datasets and models will be released to advance the development of UDC-VR within the community.

## References

Agustsson, E.; and Timofte, R. 2017. Ntire 2017 challenge on single image super-resolution: Dataset and study. In *CVPRW*,

126–135.

Ba, J. L.; Kiros, J. R.; and Hinton, G. E. 2016. Layer normalization. *arXiv preprint arXiv:1607.06450*.

Carion, N.; Massa, F.; Synnaeve, G.; Usunier, N.; Kirillov, A.; and Zagoruyko, S. 2020. End-to-end object detection with transformers. In *ECCV*, 213–229.

Charbonnier, P.; Blanc-Feraud, L.; Aubert, G.; and Barlaud, M. 1994. Two deterministic half-quadratic regularization algorithms for computed imaging. In *ICIP*, 168–172.

Chen, H.; Wang, Y.; Guo, T.; Xu, C.; Deng, Y.; Liu, Z.; Ma, S.; Xu, C.; Xu, C.; and Gao, W. 2021. Pre-trained image processing transformer. In *CVPR*, 12299–12310.

Ding, K.; Ma, K.; Wang, S.; and Simoncelli, E. P. 2020. Image quality assessment: Unifying structure and texture similarity. *TPAMI*, 44(5): 2567–2581.

Dosovitskiy, A.; Beyer, L.; Kolesnikov, A.; Weissenborn, D.; Zhai, X.; Unterthiner, T.; Dehghani, M.; Minderer, M.; Heigold, G.; Gelly, S.; et al. 2021. An Image is Worth 16x16 Words: Transformers for Image Recognition at Scale. In *ICLR*.

Feng, R.; Li, C.; Chen, H.; Li, S.; Gu, J.; and Loy, C. C. 2023. Generating Aligned Pseudo-Supervision from Non-Aligned Data for Image Restoration in Under-Display Camera. In *CVPR*, 5013–5022.

Feng, R.; Li, C.; Chen, H.; Li, S.; Loy, C. C.; and Gu, J. 2021. Removing diffraction image artifacts in under-display camera via dynamic skip connection network. In *CVPR*, 662–671.

Feng, R.; Li, C.; Zhou, S.; Sun, W.; Zhu, Q.; Jiang, J.; Yang, Q.; Loy, C. C.; Gu, J.; Zhu, Y.; et al. 2022. Mipi 2022 challenge on under-display camera image restoration: Methods and results. In *ECCV*, 60–77.

Geng, Z.; Liang, L.; Ding, T.; and Zharkov, I. 2022. Rstt: Real-time spatial temporal transformer for space-time video super-resolution. In *CVPR*, 17441–17451.

Goldstein, J. S.; Reed, I. S.; and Scharf, L. L. 1998. A multi-stage representation of the Wiener filter based on orthogonal projections. *TIT*, 44(7): 2943–2959.

Isola, P.; Zhu, J.-Y.; Zhou, T.; and Efros, A. A. 2017. Image-to-image translation with conditional adversarial networks. In *CVPR*, 1125–1134.

Johnson, J.; Alahi, A.; and Fei-Fei, L. 2016. Perceptual losses for real-time style transfer and super-resolution. In *ECCV*, 694–711.

Kim, T. H.; Sajjadi, M. S.; Hirsch, M.; and Scholkopf, B. 2018. Spatio-temporal transformer network for video restoration. In *ECCV*, 106–122.

Kingma, D. P.; and Ba, J. 2014. Adam: A method for stochastic optimization. *arXiv preprint arXiv:1412.6980*.

Koh, J.; Lee, J.; and Yoon, S. 2022. Bnucd: A two-branched deep neural network for restoring images from under-display cameras. In *CVPR*, 1950–1959.

Kwon, K.; Kang, E.; Lee, S.; Lee, S.-J.; Lee, H.-E.; Yoo, B.; and Han, J.-J. 2021. Controllable image restoration for under-display camera in smartphones. In *CVPR*, 2073–2082.

Liang, J.; Cao, J.; Fan, Y.; Zhang, K.; Ranjan, R.; Li, Y.; Timofte, R.; and Van Gool, L. 2022. Vrt: A video restoration transformer. *arXiv preprint arXiv:2201.12288*.

Liang, J.; Cao, J.; Sun, G.; Zhang, K.; Van Gool, L.; and Timofte, R. 2021. Swinir: Image restoration using swin transformer. In *ICCV*, 1833–1844.

Lin, J.; Cai, Y.; Hu, X.; Wang, H.; Yan, Y.; Zou, X.; Ding, H.; Zhang, Y.; Timofte, R.; and Van Gool, L. 2022. Flow-Guided Sparse Transformer for Video Deblurring. In *ICML*, 13334–13343.

Liu, Z.; Lin, Y.; Cao, Y.; Hu, H.; Wei, Y.; Zhang, Z.; Lin, S.; and Guo, B. 2021. Swin transformer: Hierarchical vision transformer using shifted windows. In *ICCV*, 10012–10022.

Luo, Z.; Li, Y.; Cheng, S.; Yu, L.; Wu, Q.; Wen, Z.; Fan, H.; Sun, J.; and Liu, S. 2022. BSRT: Improving burst super-resolution with swin transformer and flow-guided deformable alignment. In *CVPR*, 998–1008.

Nah, S.; Son, S.; and Lee, K. M. 2019. Recurrent neural networks with intra-frame iterations for video deblurring. In *CVPR*, 8102–8111.

Ranjan, A.; and Black, M. J. 2017. Optical flow estimation using a spatial pyramid network. In *CVPR*, 4161–4170.

Ronneberger, O.; Fischer, P.; and Brox, T. 2015. U-net: Convolutional networks for biomedical image segmentation. In *MICCAI*, 234–241.

Shi, W.; Caballero, J.; Huszár, F.; Totz, J.; Aitken, A. P.; Bishop, R.; Rueckert, D.; and Wang, Z. 2016. Real-time single image and video super-resolution using an efficient sub-pixel convolutional neural network. In *CVPR*, 1874–1883.

Su, S.; Delbraccio, M.; Wang, J.; Sapiro, G.; Heidrich, W.; and Wang, O. 2017. Deep video deblurring for hand-held cameras. In *CVPR*, 1279–1288.

Sundar, V.; Hegde, S.; Kothandaraman, D.; and Mitra, K. 2020. Deep atrous guided filter for image restoration in under display cameras. In *ECCVW*, 379–397.

Touvron, H.; Cord, M.; Douze, M.; Massa, F.; Sablayrolles, A.; and Jégou, H. 2021. Training data-efficient image transformers & distillation through attention. In *ICML*, 10347–10357.

Vaswani, A.; Shazeer, N.; Parmar, N.; Uszkoreit, J.; Jones, L.; Gomez, A. N.; Kaiser, Ł.; and Polosukhin, I. 2017. Attention is all you need. *NeurIPS*, 30.

Wang, H.; Zhu, Y.; Adam, H.; Yuille, A.; and Chen, L.-C. 2021. Max-deeplab: End-to-end panoptic segmentation with mask transformers. In *CVPR*, 5463–5474.

Wang, X.; Chan, K. C.; Yu, K.; Dong, C.; and Change Loy, C. 2019. Edvr: Video restoration with enhanced deformable convolutional networks. In *CVPRW*.

Wang, Z.; Bovik, A. C.; Sheikh, H. R.; and Simoncelli, E. P. 2004. Image quality assessment: from error visibility to structural similarity. *TIP*, 13(4): 600–612.

Wang, Z.; Cun, X.; Bao, J.; Zhou, W.; Liu, J.; and Li, H. 2022. Uformer: A general u-shaped transformer for image restoration. In *CVPR*, 17683–17693.

- Zhang, K.; Luo, W.; Zhong, Y.; Ma, L.; Liu, W.; and Li, H. 2018a. Adversarial spatio-temporal learning for video deblurring. *TIP*, 28(1): 291–301.
- Zhang, R.; Isola, P.; Efros, A. A.; Shechtman, E.; and Wang, O. 2018b. The unreasonable effectiveness of deep features as a perceptual metric. In *CVPR*, 586–595.
- Zheng, M.; Xing, Q.; Qiao, M.; Xu, M.; Jiang, L.; Liu, H.; and Chen, Y. 2022. Progressive training of a two-stage framework for video restoration. In *CVPR*, 1024–1031.
- Zhou, Y.; Kwan, M.; Tolentino, K.; Emerton, N.; Lim, S.; Large, T.; Fu, L.; Pan, Z.; Li, B.; Yang, Q.; et al. 2020. UDC 2020 challenge on image restoration of under-display camera: Methods and results. In *ECCVW*, 337–351.
- Zhou, Y.; Ren, D.; Emerton, N.; Lim, S.; and Large, T. 2021. Image restoration for under-display camera. In *CVPR*, 9179–9188.
- Zhou, Y.; Song, Y.; and Du, X. 2022. Modular Degradation Simulation and Restoration for Under-Display Camera. In *ACCV*, 265–282.
- Zhu, X.; Su, W.; Lu, L.; Li, B.; Wang, X.; and Dai, J. 2021. Deformable DETR: Deformable Transformers for End-to-End Object Detection. In *ICLR*.